Correlation of Microstructures and Conductivities of Ferroelectric Ceramics Using Complex Impedance Spectroscopy

2010 Jpn. J. Appl. Phys. 49 061505

(http://iopscience.iop.org/1347-4065/49/6R/061505)

Correlation of Microstructures and Conductivities of Ferroelectric Ceramics Using Complex Impedance Spectroscopy

Pin-Yi Chen[1,2], Chen-Chia Chou[1*], Tseung-Yuen Tseng[3], and Haydn Chen[4]

[1]*Department of Mechanical Engineering, National Taiwan University of Science and Technology, Taipei 10672, Taiwan*
[2]*Department of Mechanical Engineering, Ming-Chi University of Technology, Taipei 24301, Taiwan*
[3]*Department of Electronics Engineering and Institute of Electronics, National Chiao-Tung University, Hsinchu 300, Taiwan*
[4]*Department of Physics, Tunghai University, Taichung 407, Taiwan*

Received January 12, 2010; accepted February 12, 2010; published online June 21, 2010

The microstructures and conductivities of lead-free ceramics $[Bi_{0.5}(Na_{1-x}K_x)_{0.5}]TiO_3$ with $x = 0.18$ (BNKT) and lead-based ceramics of $x(0.94PbZn_{1/3}Nb_{2/3}O_3 + 0.06BaTiO_3) + (1 - x)PbZr_yTi_{1-y}O_3$ with $x = 0.5$, $y = 0.52$ (PBZNZT) were investigated. Experimental results show that the activation energy of grain boundary conductivity is higher than that of grain conductivity for the BNKT system, indicating that the Bi_2O_3 evaporation of grains induces an easy conduction path through grains. However, the activation energy of grain boundary conductivity is lower than that of grain conductivity for the PBZNZT system, which might be attributed to the charged particles in the amorphous phase at grain boundaries, participating in the conduction process. A conduction model of both grain and grain boundary conductivities was proposed, and the microstructural characteristics and AC impedance data of ferroelectric ceramics correlate fairly well, suggesting that impedance spectroscopy is an efficient characterization technique for the grain boundary engineering of ferroelectric ceramics.

DOI: 10.1143/JJAP.49.061505

1. Introduction

In recent years, lead zirconate titanate-lead zinc niobate $Pb(Zr_{1/2}Ti_{1/2})O_3$–$Pb(Zn_{1/3}Nb_{2/3})O_3$ (PZT–PZN) piezoelectric materials have been widely applied in piezoelectric actuators, sensors, and transducers owing to their excellent dielectric, piezoelectric, and ferroelectric properties.[1–3] However, perovskite PZN has been reported to be thermodynamically unstable over a wide range of temperatures of 600–1400 °C.[4] A useful method of stabilizing the perovskite structure is to use additives such as $BaTiO_3$ (BT) and $SrTiO_3$ (ST). For example, a small increase in the amount of BT stabilizes PZN.[5,6] However, the phase transformation temperature of PZN may become lower than the room temperature. Accordingly, other stabilizers must be added to raise the ferroelectric–paraelectric phase transformation temperature. $PbTiO_3$ (PT)–$PbZrO_3$ (PZ) is commonly employed to adjust those properties. Recently, many countries have restricted the use of lead oxide by drafting legislations because of the toxicity of the compound and its high vapor pressure during processing as well as the harm poses to the environment and human health. Thus, it is necessary and urgent to search for lead-free piezoelectric ceramics with excellent ferroelectric and piezoelectric properties.[7]

$Bi_{0.5}Na_{0.5}TiO_3$ (BNT) is considered to be a potential candidate lead free piezoelectric ceramic with its relatively large remanent polarization ($P_r = 38\,\mu C/cm^2$) and high Curie temperature ($T_c = 320\,°C$).[8–10] However, BNT has drawbacks of high conductivity and high coercive field E_c, which can cause problems in the poling process.[11] BNT-based solid solutions have been studied and some BNT-based lead-free piezoelectric ceramics systems with good piezoelectric properties have been reported, such as BNT–$BaTiO_3$, BNT–$Bi_{0.5}K_{0.5}TiO_3$, BNT–$BaTiO_3$–$Bi_{0.5}K_{0.5}TiO_3$, BNT–$(Na,K)NbO_3$, BNT–$Ba(Ti,Zr)O_3$, and BNT–$BiLiTiO_3$–$Bi_{0.5}K_{0.5}TiO_3$.[12–17] Among these materials, the $(1 - x)$ BNT–xBKT system with relatively good piezoelectric and dielectric properties can be obtained near the rhombohedral–tetragonal morphotropic phase boundary (MPB) with $x = 0.16–0.20$. Since $Bi_{0.5}K_{0.5}TiO_3$ can be partially substituted for BNT, E_c can be reduced. Higher electromechanical coupling factor (K_p) and dielectric constant (ε_r) were observed around the MPB region.

A serious problem with BNT-based ceramics is theirs large leakage current, which often correlates with the vaporization of Bi during sintering, and the subsequent defect formation at high temperatures.[18] Defects strongly affect leakage current behavior in ferroelectric ceramics, which also affect dielectric, ferroelectric, and piezoelectric properties. On the other hand, microstructural characteristics affect transport properties in polycrystalline ceramics. Impedance spectroscopy (IS) has been thought as an effective technique for the study of materials in terms of not only their electrical application but also their microstructures and phase transition information. However, only a few impedance studies have been performed in BNT- and PZN-based piezoelectric ceramics to determine the correlation of what with microstructural characteristics. Therefore, the purpose of this work is to investigate the microstructural differences of grains and grain boundaries between BNT- and PZN-based ceramics using electron microscopy and to determine the correlation of what with electrical conductivity by complex impedance analysis.

2. Experimental Procedure

Specimens of $x(0.94PbZn_{1/3}Nb_{2/3}O_3 + 0.06BaTiO_3) + (1 - x)PbZr_yTi_{1-y}O_3$ (abbreviated as PBZNZT) with $x = 0.5$ and $y = 0.52$ were fabricated in this experiment. PbO, ZnO, Nb_2O_5, ZrO_2, $BaCO_3$, and TiO_2 were used as the starting raw materials. The specimens were prepared by the A-site-element sequential mixing columbite (ASMC) method.[19–22] Following calcination, the reground powders were pressed into discs with a diameter of 10 mm and a thickness of 1 mm. The sintering process was performed at 1150 °C for 2 h using a double crucible that contained $PbZrO_3$ powder to prevent the evaporation of PbO. Lead-free $[Bi_{0.5}(Na_{1-x}K_x)_{0.5}]TiO_3$ (abbreviated as BNKT) ceramics with $x = 0.18$ using conventional solid state reaction were also fabricated. Reagent-grade oxide and carbonate

*E-mail address: ccchou@mail.ntust.edu.tw

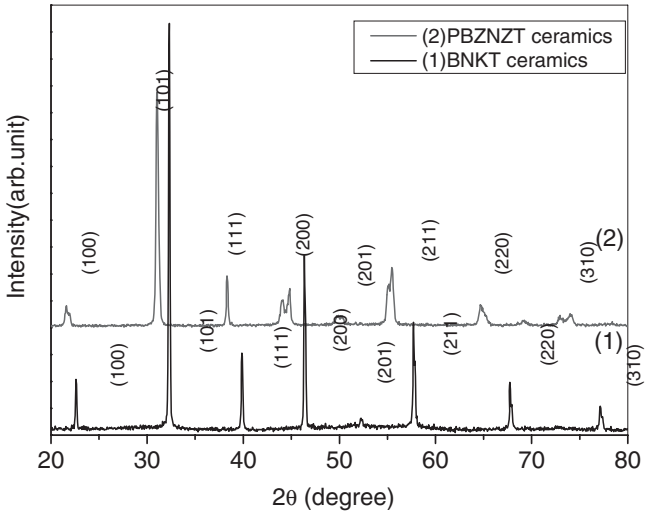

Fig. 1. XRD patterns of BNKT and PBZNZT sintered specimens.

powders such as Bi_2O_3, Na_2CO_3, K_2CO_3, and TiO_2 were used as the starting raw materials. All powders were ball-milled for 24 h and calcined at 850 °C for 2 h. The calcined powders were also reground and pressed into disc specimens with a diameter of 10 mm and a thickness of 1 mm. The green discs were sintered at 1150 °C for 2 h using a crucible containing calcined BNKT powders to prevent the evaporation of Bi_2O_3, Na_2O, and K_2O. All the specimens was polished to a thickness of 0.6 mm, and silver paste was applied as the electrode and baked at 650 °C for 30 min to facilitate electrical measurement. X-ray diffraction (XRD) analysis (Rigaku Max-RC) was used to determine the crystal phase of the samples. Micrographs of the prepared samples were obtained using a scanning electron microscopy (SEM; JEOL FESEM 6500F). Density was measured by the Archimedes method using distilled water. A Solartron 1260 AC impedance analyzer was used to measure impedance plots from 300 to 700 °C in the frequency range of 0.1 Hz–1 MHz.

3. Results and Discussion

The relative density of the sintered samples was higher than 95% of their theoretical values. Therefore, the effect of porosity on conductivity can be neglected in the following analysis. Figure 1 shows the XRD patterns of the BNKT and PBZNZT specimens. The pyrochlore phase was very easily formed in the PZN material system. PBZNZT ceramics were prepared using the ASMC method, which effectively minimizes pyrochlore phase generation.[19,20] On the other hand, the patterns of BNKT ceramics primarily exhibited a perovskite tetragonal structure, as shown in Fig. 1. We compared the crystal structures of the as-sintered BNKT and PBZNZT specimens. The c/a ratios of the tetragonal phase are 1.006 and 1.013 Å, respectively. PBZNZT ceramics clearly display a larger tetragonality.

To compare the microstructures and electrical properties of the BNKT and PBZNZT ceramics, we utilized impedance spectroscopy and electron microscopy to determine the correlation of electrical properties and microstructures. Transmission electron microscopy (TEM) was performed to understand the microstructural characteristics of the specimens. Figure 2 shows high-resolution TEM (HRTEM) images of grain boundaries in the BNKT and PBZNZT specimens. The BNKT specimens show clean and thin grain boundaries without elemental segregation, as shown in Figs. 2(a) and 2(b). A thin grain boundary layer with a distorted lattice resulting in an image contrast with a thickness of approximately 5 nm was observed. The results of the composition analysis of TEM equipped with energy dispersive X-ray spectrometer (TEM–EDS) at the grain boundary are shown in Table I; the results are also similar to those of the grain interior. On the other hand, images of the PBZNZT specimens exhibit an amorphous phase at grain boundaries with a thickness of approximately 15 nm, as shown in Figs. 2(c) and 2(d). It was reported that PbO might segregate to form an amorphous layer or second phases at grain boundaries.[19–23] A semiquantitative TEM–EDS study of the grain boundary showed that grain boundaries possess large amounts of PbO and ZnO, as shown in Table I. The result indicates that PbO and ZnO form an intergranular layer in the present PBZNZT material system.

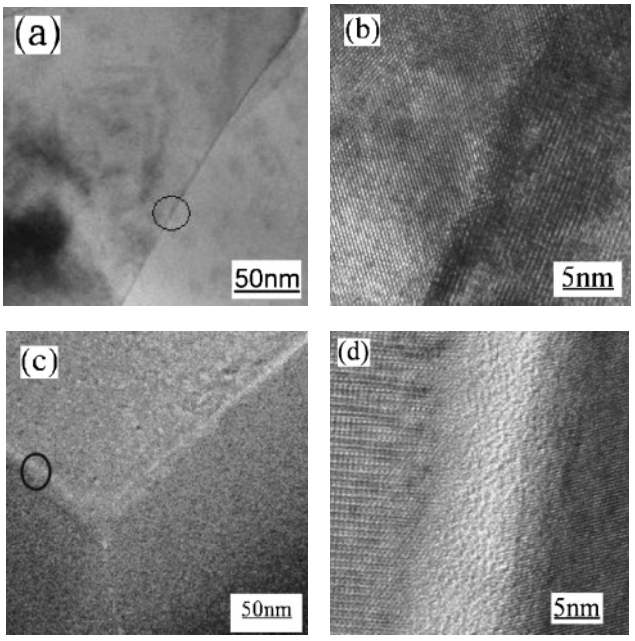

Fig. 2. Atomic structure images of grain boundaries in (a,b) BNKT and (c,d) PBZNZT specimens.

Table I. Results of TEM–EDS elemental analyses of grain boundaries for (a) PBZNZT and (b) BNKT samples (unit: at. %).

(a)

Pb	Ti	Zn	Zr	Nb
44.8	7.2	44.6	1.9	1.6

(b)

Bi	Na	K	Ti	O
18	8	0.8	22	52

SEM investigations of specimen microstructures and fracture surface may provide useful information about materials. The grain sizes of the BNKT and PBZNZT ceramics were estimated using the ASTM standard to be 1.47 and 2.1 μm, respectively. The BNKT ceramics displayed transgranular-type of fracture as shown in Fig. 3(a).

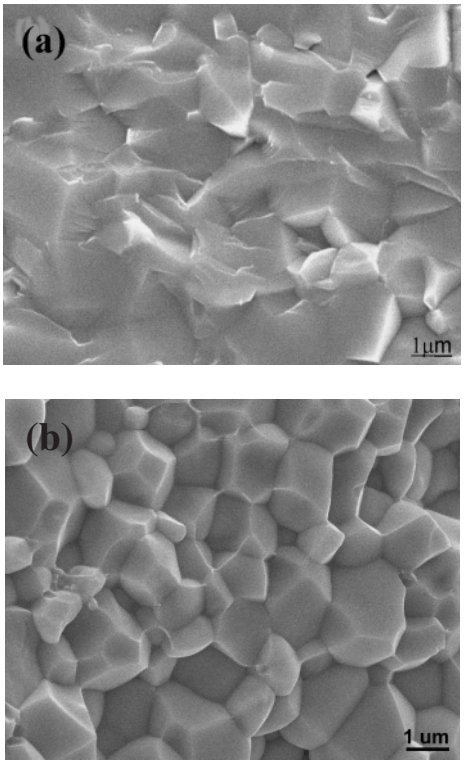

Fig. 3. SEM images of fracture surface for (a) BNKT and (b) PBZNZT samples.

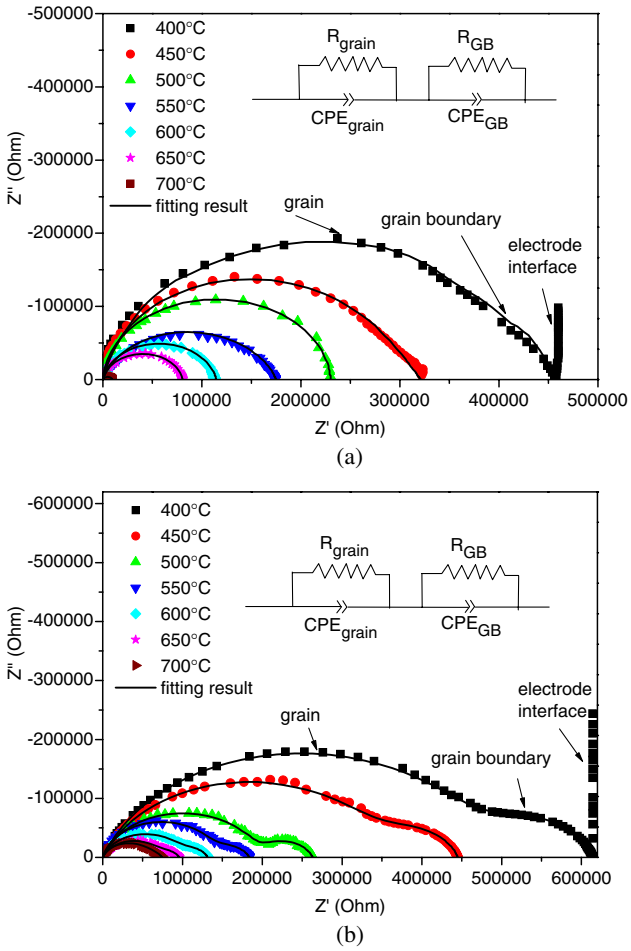

Fig. 4. (Color online) Complex impedance plots of (a) BNKT and (b) PBZNZT ceramics measured in the range of temperatures of 400 to 700 °C and experimental impedance spectra simulated by the corresponding equivalent circuit.

This implies that the strength of grain boundaries is higher than that of grains in BNKT ceramics. This may be attributed to the evaporation of Bi_2O_3 during the sintering of the BNKT ceramics at 1150 °C for 2 h, which reduces the grain strength of materials. On the other hand, SEM images of the fracture surface of the PBZNZT ceramics clearly displayed intergranular fracture, as shown in Fig. 3(b). This result suggests that a weaker continuous phase, which can be attributed to the segregation of PbO and ZnO that leads to an amorphous phase, fractures along grain boundaries for the PBZNZT ceramics. The microstructural feature of the BNKT ceramics with a thin grain boundary is quite different from that of the PBZNZT ceramics with a continuous amorphous layer at grain boundaries.

Complex impedance plots were measured in the frequency range from 0.1 Hz to 1 MHz at different temperatures. When impedance was measured below 350 °C, the data become divergent and irregular. The impedance plots were therefore analyzed in the temperature range of 400 to 700 °C. Figure 4(a) shows impedance spectroscopic plots of the BNKT ceramics, which show only one semicircle in the measuring frequency range. This indicates that the contribution of grain boundary to conductivity is not evident at higher temperatures. Bauerle[24] and Schouler *et al.*[25] proposed the different models to interpret conduction behavior of an yttria-stabilized zirconia electrolyte, which suggest that clean grain boundaries of grain-to-grain contact provided an easy path for mobile charge transport in materials at higher temperatures, if ionic conduction predominates. According to our TEM observation, BNKT ceramics present no amorphous layer at grain boundaries and form grain-to-grain contact. This might produce a convenient path for ion transport grain by grain through thin grain boundaries at high temperatures. On the other hand, the complex impedance plots for the PBZNZT specimens in Fig. 4(b), clearly indicate two semicircles representing the impedances of grains and grain boundaries, respectively. The high-frequency semicircle represents the impedance of grains and the low-frequency one indicates the impedance of grain boundaries. The results show a significant conductivity difference between PBZNZT and BNKT specimens.

In order to quantitatively analyze resistances at grains and grain boundaries, experimental impedance spectra were simulated using a corresponding equivalent circuit with two parallel R–C elements in series. Therefore, R_g and R_{gb} at each test temperature were extracted and then converted into conductivities (σ) using

$$\sigma = \frac{t}{S \times R}, \tag{1}$$

where t is the sample thickness and S is the electrode area in the sample surface. We obtain apparent grain conductivity $(\sigma_g)_a$, and the conductivity follows the Arrhenius law; the value determined from R_g can be treated approximately as the true σ_g, because of the negligible thickness of the grain boundary layer in the sample. However, the apparent grain boundary conductivity $(\sigma_{gb})_a$ cannot give insight into the grain boundary effect since the area of grain boundary

Table II. Grain-boundary conductivities σ_{gb} calculated from data of AC impedance.

	R_g (Ω cm^2)	R_{gb} (Ω cm^2)	$(\sigma_{gb})_a$ (S/cm)	ω_g (Hz)	ω_{gb} (Hz)	d/L^*	σ_{gb} (S/cm)
PBZNZT							
400 °C	482000	132300	9.82×10^{-7}	3981.07	109.79	0.00757	7.43×10^{-9}
450 °C	353000	92020	1.41×10^{-6}	5495.41	169.50	0.00804	1.14×10^{-8}
500 °C	196500	66500	1.95×10^{-6}	1778.28	46.60	0.00887	1.73×10^{-8}
550 °C	138630	45170	2.88×10^{-6}	1096.48	26.92	0.00800	2.30×10^{-8}
600 °C	99250	32150	4.04×10^{-6}	1778.28	43.65	0.00795	3.21×10^{-8}
650 °C	70900	25000	5.20×10^{-6}	3388.44	70.79	0.00737	3.83×10^{-8}
700 °C	54780	19700	6.60×10^{-6}	2884.03	60.26	0.00751	4.96×10^{-8}
BNKT							
400 °C	345000	115000	1.13×10^{-6}	1714.82	22.91	0.00445	5.03×10^{-9}
450 °C	250000	71000	1.83×10^{-6}	1134.92	14.13	0.00354	6.47×10^{-9}
500 °C	155000	65500	1.98×10^{-6}	1478.28	15.82	0.00452	8.97×10^{-9}
550 °C	130000	45000	2.89×10^{-6}	1225.48	15.46	0.00437	1.26×10^{-8}
600 °C	90000	24500	5.30×10^{-6}	1278.28	16.65	0.00355	1.88×10^{-8}
650 °C	70000	10500	1.24×10^{-5}	1388.44	29.79	0.00322	3.98×10^{-8}
700 °C	8000	1500	8.66×10^{-5}	884.03	15.89	0.00337	2.92×10^{-7}

$* \; d/L = \omega_g R_g / \omega_{gb} R_{gb}$

parallel to the current flow is much smaller than that of the grain.[26] The calculation of the true grain boundary conductivity σ_{gb} requires different geometrical factors. Wang and Nowick[27] proposed the true grain-boundary conductivity σ_{gb}, which can be modified by a geometrical factor and can be defined as

$$\sigma_{gb} = \frac{d}{L \times (\sigma_{gb})_a}, \tag{2}$$

where d is the thickness of the grain-boundary layer and L is the average grain size. The ratio d/L is not easily obtained without extensive microstructure measurements. However, a simple method was developed in previous studies[28,29] to estimate d/L by complex impedance measurements. A simple analysis of the relationships between the resistance R, the capacitance C, the permittivity ε, and the geometry of the test sample yields the following relation[28,29]

$$\frac{C_g}{C_{gb}} = \left(\frac{\varepsilon_g}{\varepsilon_{gb}}\right)\frac{d}{L}, \tag{3}$$

where the subscripts "g" and "gb" denote grain and grain boundary, respectively. It is generally assumed[28,29] that $\varepsilon_g/\varepsilon_{gb} \approx 1$. On the other hand, $\omega RC = 1$ at the top of each arc of the measured complex impedance plots. Thus, we can readily obtain the ratio d/L using the characteristic frequency ω and the resistance R

$$\frac{d}{L} \approx \frac{\omega_{gb} R_{gb}}{\omega_g R_g}. \tag{4}$$

The characteristic frequencies ω_g and ω_{gb}, and the resistances R_g and R_{gb} can be determined easily from complex impedance plots. Using these data, the ratio d/L was estimated using eq. (4). It was estimated that the ranges of $(d/L)_{BNKT}$ and $(d/L)_{PBZNZT}$ are approximately 0.0032 to 0.0045 and 0.0074 to 0.0089, respectively. The corresponding d values for the grain boundaries of the BNKT and PBZNZT ceramics with average grain sizes of 1.47 and 2.10 μm are therefore estimated to be approximately 4.7 to 6.6 nm and 15 to 19 nm, respectively. We found that the microstructural characteristics estimated using impedance spectroscopy correlate well with the results obtained using electron microscopy in the present ferroelectric materials, as shown in Fig. 2.

The apparent grain-boundary conductivities $(\sigma_{gb})_a$ obtained from R_{gb} using eq. (1) and the true grain-boundary conductivities σ_{gb} were calculated using eq. (2) for each sample at different temperatures. The conductivities and corresponding microstructural data are listed in Table II. Since we are able to measure the conductivities of the grains and grain boundaries, and evaluate grain boundary thickness and characteristics as well, it appears that impedance spectroscopy can be employed for the grain boundary engineering of materials.

Figure 5 shows the values of σ_g and σ_{gb} for the test samples as a function of test temperature in BNKT and PBZNZT specimens, respectively. The results demonstrate that the conductivity of grains is about two orders of magnitude higher than that of grain boundaries in BNKT and PBZNZT specimens, if we consider the dimension of grain boundaries, implying that the conductivity of grains plays a major role in leakage behavior. We also calculated the activation energy for grain (E_g) conduction and grain boundary (E_{gb}) conduction. The activation energies of grain and grain boundary in the BNKT specimens were 1.73 and 2.09 eV, respectively. This result shows that the activation energy of the grain boundary is higher than that of the grain in the BNKT materials, implying that bismuth oxide evaporation during sintering reduces the height of the moving barrier of charges in grains. On the other hand, the activation energies of grain and grain boundary in PBZNZT specimens were calculated to be 2.12 and 1.79 eV, respectively. This result shows that activation energy of the grain boundary is lower than that of the grain. A reasonable explanation for this is the fact that a transient liquid-phase sintering primarily using lead and zinc oxide species can lead to formation of grain boundary amorphous phases, which produce charged defects during sintering at grain boundaries. Thus, during AC impedance measure-

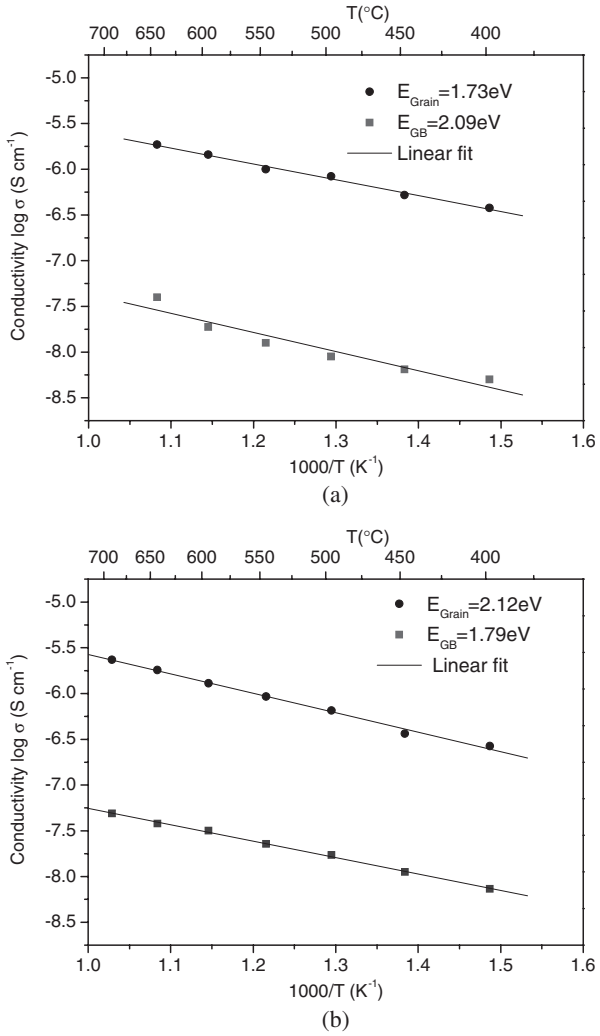

Fig. 5. Variations in total conductivity with inverse of temperature ($1/T$) for BNKT and PBZNZT samples.

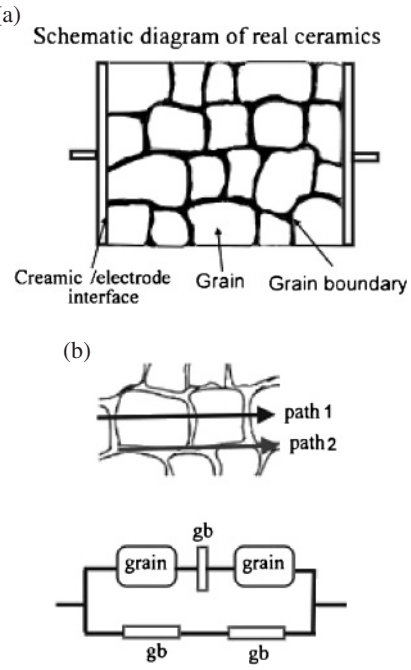

Fig. 6. Conductivity models proposed for BNKT and PBZNZT ceramics considering grains and grain boundaries: (a) microstructures of real ceramics and (b) conduction routes with two parallel paths, i.e., path 1 through grains across grain boundaries, and path 2 along grain boundaries.

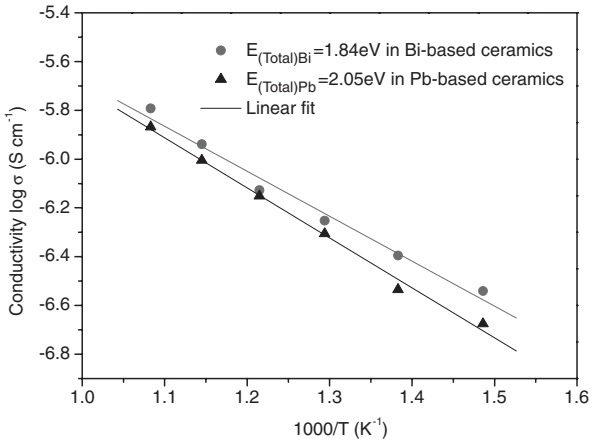

Fig. 7. Variations in total conductivity with inverse of temperature ($1/T$) for BNKT and PBZNZT samples.

ments at high temperatures, the charged species in the grain boundary glassy phase may participate in the conduction process. It turns out that the grain boundary resistivity R_{gb} decreased with increasing measurment temperature.

To interpret the current impedance data with microstructural characteristics, we show a brick layer model combined with conduction paths in Fig. 6. Figure 6(a) showed microstructures of real ceramics containing grains, grain boundaries, and interfaces between ceramics and electrodes.[30] Figure 6(b) shows two parallel paths available for conduction which is either through grains and across grain boundaries or along grain boundaries. Path 1 represents the transport route through grains and across grain boundaries, and path 2 represents the route where charged particles can move along grain boundaries. Because grain boundaries occupy only a small fraction of a material, we may assume grain boundaries to have a thickness d_{GB}, where d_{GB} is very thin. Note that the resistance of grain boundaries is relatively small compared with that of grains. Current flow is assumed to be one-dimensional, and the curvature of flow paths at the corners of the grains is negligible. Since the grain boundary conductivity is relatively smaller than the grain conductivity, current flow path 2 can be neglected, and path 1 can be simplified in two parallel R–C elements representing in series grains and grain boundaries, which is consistent with the RC model used in impedance analysis.

In order to estimate conductivity of total bulk, total bulk resistance (R_{total}) was obtained from the intercept of the semicircle on the real axis (Z') in the complex plots. The R_{total} at each test temperature was converted into total conductivity (σ_{total}) using eq. (1). Conductivity follows the Arrhenius law, and activation energy can be calculated from the slope of the linear portion of the σ vs $10^3/T$ graph. The total activation energy $(E_{total})_{BNKT}$ was estimated as 1.84 eV and $(E_{total})_{PBZNZT}$ was calculated to be 2.05 eV, as shown in Fig. 7. Here, it was found that the total activation energy $(E_{total})_{BNKT}$ of BNKT ceramics is lower than the $(E_{total})_{PBZNZT}$ of PBZNZT ceramics. Volatile elements such as Bi and Pb are easier to evaporate at higher sintering

temperatures which results in the formation of oxygen vacancies. However, the vapor pressure of bismuth oxide is higher than that of lead oxide,[31] implying that bismuth oxide in BNKT ceramics is easier to vaporize than lead oxide in PBZNZT ceramics. Therefore, BNKT ceramics might exhibit more oxygen vacancies and therefore more pronounced ion movement. This might be the reason why the activation energy is lower for BNKT ceramics than for PBZNZT ceramics; therefore, BNKT exhibits a larger leakage current.

4. Conclusions

Impedance spectroscopy studies have been successfully performed in BNKT and PBZNZT piezoelectric ceramics to determine the correlation between microstructures and electrical conduction behavior. The results indicate that the difference in microstructure between BNKT and PBZNZT ceramics reflects the distinct difference in conductivity behavior between these materials.

BNKT ceramics exhibit clean and thin grain boundaries and a transgranular fracture surface. Impedance analysis of these ceramics shows only one semicircle in complex impedance plots, and the contribution of grain boundaries is not evident at higher temperatures. The activation energy of grain boundary conductivity is higher than that of grain conductivity for the BNKT system, indicating that the Bi_2O_3 evaporation of grains induces an easy conduction path through grains in BNKT ceramics.

On the other hand, PBZNZT ceramics exhibit a thick amorphous layer at grain boundaries and intergranular-type fracture. Impedance analysis of these ceramics clearly shows two semicircles in complex impedance plots, and the activation energy of grain boundary conductivity is lower than that of grain conductivity for the PBZNZT system. This might be attributed to the charged particles in the amorphous phase at grain boundaries participating in the conduction process at high temperatures.

A conduction model based on microstructures considering both grain and grain boundary conductivities was proposed. Grain boundary thickness was calculated through AC impedance data and compared with results of the electron microscopic investigation. It was found that the microstructural characteristics and AC impedance data of ferroelectric ceramics correlate fairly well, suggesting that impedance spectroscopy can be employed in grain boundary engineering of ferroelectric ceramics.

Acknowledgement

The authors acknowledge the financial provided by the National Science Council of Taiwan for project No. 97-2923-M-029-001-MY3.

1) N. Vittayakorn, G. Rujijanagul, T. Tunkasiri, X. Tan, and D. P. Cann: J. Mater. Res. **18** (2003) 2882.
2) H. Fan and H. E. Kim: J. Appl. Phys. **91** (2002) 317.
3) N. Vittayakorn, G. Rujijanagul, X. Tan, H. He, M. A. Marquardt, and D. P. Cann: J. Electroceram. **16** (2006) 141.
4) S. Y. Chen, C. M. Wang, and S. Y. Cheng: Mater. Chem. Phys. **52** (1998) 207.
5) A. Halliyal, U. Kumar, R. E. Newnham, and L. E. Cross: J. Am. Ceram. Soc. **70** (1987) 119.
6) J. R. Belsick, A. Halliyal, U. Kumar, and R. E. Newnham: Am. Ceram. Soc. Bull. **66** (1987) 664.
7) T. Takenaka and H. Nagata: J. Eur. Ceram. Soc. **25** (2005) 2693.
8) T. Takenaka, K. Maruyama, and K. Sakata: Jpn. J. Appl. Phys. **30** (1991) 2236.
9) T. Takenaka and K. Sakata: Ferroelectrics **95** (1989) 153.
10) H. Nagata and T. Takenaka: Jpn. J. Appl. Phys. **36** (1997) 6055.
11) A. Sasaki, T. Chiba, Y. Mamiya, and E. Otsuki: Jpn. J. Appl. Phys. **38** (1999) 5564.
12) L. Wu and D. Xiao: Jpn. J. Appl. Phys. **46** (2007) 7382.
13) Y. Hiruma, K. Yoshii, H. Nagata, and T. Takenaka: J. Appl. Phys. **103** (2008) 084121.
14) Y. Hiruma, H. Nagata, and T. Takenaka: Jpn. J. Appl. Phys. **45** (2006) 7409.
15) G. Fan, W. Lu, X. Wang, and F. Liang: Appl. Phys. Lett. **91** (2007) 202908.
16) Y. Q. Yao, T. Y. Tseng, C. C. Chou, and H. Chen: J. Appl. Phys. **102** (2007) 094102.
17) C. W. Tai, S. H. Choy, and H. L. W. Chan: J. Am. Ceram. Soc. **91** (2008) 3335.
18) R. Zuo, S. Su, Y. Wu, J. Fu, M. Wang, and L. Li: Mater. Chem. Phys. **110** (2008) 311.
19) C. L. Li and C. C. Chou: Integrated Ferroelectr. **50** (2002) 101.
20) C. L. Li and C. C. Chou: J. Eur. Ceram. Soc. **26** (2006) 1237.
21) B. M. Song, D. Y. Kim, S. I. Shirasaki, and H. Yamamura: J. Am. Ceram. Soc. **72** (1989) 833.
22) H. M. Jang and K. M. Lee: J. Mater. Res. **9** (1994) 2634.
23) M. Villegas, J. F. Fernandez, A. C. Caballero, Z. Samardija, G. Drazic, and M. Kosec: J. Mater. Res. **14** (1999) 898.
24) J. E. Bauerle: J. Phys. Chem. Solids **30** (1969) 2657.
25) E. Schouler, G. Girond, and M. Kleitz: J. Chem. Phys. **70** (1973) 1309.
26) R. Gerhardt: J. Phys. Chem. Solids **55** (1994) 1491.
27) D. Y. Wang and A. S. Nowick: J. Solid State Chem. **35** (1980) 325.
28) C. Tian and S. W. Chan: Solid State Ionics **134** (2000) 89.
29) R. Gerhardt and A. S. Nowick: J. Am. Ceram. Soc. **69** (1986) 641.
30) T. V. Dijk and A. J. Burggraaf: Phys. Status Solidi A **63** (1981) 229.
31) Y. Wu and G. Cao: Appl. Phys. Lett. **75** (1999) 2650.